ELSEVIER

Contents lists available at ScienceDirect

Materials Science & Engineering A

journal homepage: www.elsevier.com/locate/msea





Influence of accelerated corrosion on Al/steel RSW joints by *in situ* compression tests

Bo Pan ^a, Hui Sun ^b, Dongyue Xie ^c, Shun-Li Shang ^b, Nan Li ^c, Blair E. Carlson ^d, Yumeng Li ^e, Zi-Kui Liu ^{b, *}, Jingjing Li ^{a, **}

- ^a Department of Industrial and Manufacturing Engineering, The Pennsylvania State University, University Park, PA, 16802, USA
- ^b Department of Materials Science and Engineering, The Pennsylvania State University, University Park, PA, 16802, USA
- ^c Center for Integrated Nanotechnologies, Los Alamos National Laboratory, Los Alamos, NM, 87545, USA
- ^d Manufacturing Systems Research Laboratory, Global Research and Development, General Motors LLC, Warren, MI, 48092, USA
- e Department of Industrial and Enterprise Systems Engineering, University of Illinois at Urbana- Champaign, Urbana, IL, 61801, USA

ARTICLE INFO

Keywords: Dissimilar resistance spot welding Intermetallic compound Al/steel joint Corrosion mechanism Micropillar compression Crack initiation and propagation

ABSTRACT

The present work investigates the correlations between galvanic corrosion, intermetallic compound (IMC) formation, and the input of welding energy with respect to the initiation and propagation of micro-cracks in micropillars of resistant spot welding (RSW) joints between aluminum (Al) and steel. The present results indicate that, in the high welding energy region, Al was corroded first after 26 cycles of corrosion, and Al₅Fe₂ IMC was corroded after 72 cycles of corrosion due to its high corrosion potential predicted by the calculations based on density functional theory (DFT) in terms of the Nernst equation. In comparison with the high welding energy region, less corrosion was observed in the middle welding energy region due to the thinner Al₅Fe₂ IMC layer, a lower amount of Al₁₃Fe₄ IMC in the Al matrix, and lower residual stress. Mechanical properties at different locations after various corrosion conditions were obtained using in situ compression tests, including the stressstrain responses and the strain rate sensitivity. The micropillars from the high welding energy region have a higher average yielding stress due to the thicker IMC layer than those from the middle welding energy region. The yielding stress decreases gradually with increasing corrosion cycles. Three conditions for crack initiation and propagation have been identified: firstly, for pillars from the high welding energy region before corrosion or the middle welding energy region (before or under the minimal corrosion conditions), the cracks initiate within the IMC layer; secondly, for pillars from the high welding energy region after 26 cycles of corrosion (under the moderate corrosion condition), cracks propagate at the Al/IMC interface; finally, for pillars from the high welding energy region after 72 cycles of corrosion (under the severe corrosion condition), the cracks initiate at the IMC/steel interface.

1. Introduction

Compared to traditional vehicle bodies manufactured solely from steel, hybrid bimetal Al/steel structures have become increasingly popular in the automotive industry due to the combined advantages of both metals [1–5]. Al has high corrosion resistance, while steel offers high strength and ease of manufacturing [6,7]. To join Al and steel alloys, various welding methods such as RSW, laser welding [8], friction stir welding [9,10], and explosive welding [6], as well as mechanical joining methods such as self-piercing riveting [11], are applied in the

production of Al/steel dissimilar joints. Among these approaches, RSW is a preferred method for joining Al and steel in the automotive and aerospace industries due to its low cost, ease of automation, and high efficiency [12,13].

Most research on Al/steel RSW joints focused on welding parameters, bonding strength, interfacial behavior, and fracture mechanisms [14–17], with limited research on corrosion behavior [18]. Corrosion behavior is a significant factor in evaluating the quality of welding joints, particularly for Al/steel joints, where the IMC layers are formed at the interface of Al and steel, significantly affecting the corrosion

E-mail addresses: zxl15@psu.edu (Z.-K. Liu), jul572@psu.edu (J. Li).

^{*} Corresponding author.

^{**} Corresponding author.

behavior of the joint. Qiu et al. [14] and Wan et al. [15] reported that the IMC layers consisted of columnar Al₅Fe₂ grains and needle-like Al₁₃Fe₄ grains. The thermal history of the welding process greatly affects the type, thickness, and morphology of IMC layers, complicating the analysis of the corrosion mechanism. The corrosion behavior of Al/steel joints includes the galvanic corrosion that occurred at the Zn coating on the steel, Al alloy, and steel sheet [12], the localized corrosion generated at the IMC phases between the Al and steel [16,17], and the corrosion generated from the secondary phases' precipitation in the Al and weld seam [19]. Lim et al. [20] investigated the corrosion behavior of the friction bit joint of AA7075 Al alloy and DP 980 steel and found that the Zn coating on the steel protected the steel from galvanic corrosion. Shi et al. [21] identified that the IMCs formed at the interface contributed to the galvanic corrosion of the adjacent weld seam and decreased the corrosion resistance of the dissimilar materials 1060 Al and Q235 steel joint. Sravanthi et al. [22] found that the Al-Fe and Al-Fe-Si alloys suffered the major deterioration of corrosion resistance in Al/steel joints, while the Al-Mg-Si precipitates were the major reason for weight loss in the Al alloy. Ma et al. [23] investigated the influence of IMC on the corrosion behavior of Al/steel hybrid fusion-brazed joints and observed the pitting holes on the IMC layers when the heat input was lower than 652 J/cm due to the galvanic corrosion between IMCs (anode) and steel (cathode). When the heat input was higher than 652 J/cm, severe corrosion was observed between IMCs and the weld seam due to the galvanic difference between the weld seam and the IMCs, while the IMCs were sheltered from corrosion. Ma et al. [24] investigated the influence of IMCs on the corrosion behavior of Al/steel hybrid fusion-brazed PX-Al and ST06 Z steel gas tungsten arc welding joints and found that the corrosion behavior of the joint was dominated by the incomplete corrosion products (such as ZnO and Al2O3) and the secondary phases (such as the Al-Si-Mn-Fe phases, Al₅Fe₂, and Al₁₃Fe₄).

Mechanical properties are essential factors in evaluating the impact of corrosion on the performance of dissimilar material joints [25]. Compared to standard mechanical testing, micro-scale mechanical testing allows the investigations of effects of microstructural features and *in situ* atomic-scale or micro-scale structural characterization [26, 27], for example, single-crystal lacking strain gradients [28], crystals with different orientations [29], and the nanoscale eutectics structure [30].

In the present work, corrosion behaviors of Al/steel RSW joints after different heat input conditions and corrosion cycles were investigated through experimental characterizations, finite element analysis, and thermodynamic calculations. Micropillar compression was employed to study the effects of corrosion on mechanical effects. The present work aims to establish a relationship between mechanical properties, deformation morphology, crack initiation and propagation, and salt spray corrosion of Al/steel RSW joints.

2. Experimental procedure

2.1. Materials, RSW process, and accelerated corrosion tests

An AA6022-T4 Al alloy sheet (137 mm \times 38 mm \times 1.2 mm) and an HSLA 340 galvanized steel sheet (137 mm \times 38 mm \times 2 mm) were joined using the RSW method, and the overlap region is 38 mm \times 38 mm. The compositions of the AA6022 and HSLA 340 alloys are given in Table 1.

The RSW process was presented in a previous study [31]. Before

Table 1 Chemical compositions (wt.%) of AA6022 Al and HSLA 340 galvanized steel.

Elements	Si	Fe	Mn	Zn	Cu	Mg	Al
AA6022 Elements HSLA 340	1.3 C 0.12	0.14 Si 0.5	0.07 Mn 1.5	0.23 Ti 0.15	0.07 Fe Bal.	0.65	Bal.

welding, the AA6022 Al and HSLA 340 steel sheets were cleaned using abrasive paper and acetone. The RSW joint was then prepared using a direct current (DC) welding machine (Milco Weld System, manufactured by Milco Manufacturing in Warren, MI), with the Al and steel sheets connected to the positive and negative electrodes, respectively. The holding force for the welding process was 900 lb (408.233 kg), and the welding process consisted of a preheating stage and two welding stages, with the welding parameters provided in the previous study [32].

To assess the corrosion resistance of the Al/steel RSW joints, salt spray corrosion tests were conducted at the Corrosion Engineering Laboratory in General Motors R&D. The salt spray solution, in accordance with the GMW14872 standard [25], was composed of 0.90 wt% NaCl, 0.10 wt% CaCl₂, and 0.075 wt% NaHCO₃, with a pH range of 6.1–6.5. Each accelerated corrosion test cycle lasted for 24 h with an 8-h ambient stage, an 8-h humid stage, and an 8-h dry-off stage (the details are presented in the former study [33]). The corrosion tests were conducted for 7, 26, and 72 cycles, with all five specimens under each corrosion condition exhibiting similar behavior after the corrosion tests. One specimen from each condition was selected for future characterization.

2.2. Microstructure characterization and mechanical tests of micro-pillars

After the corrosion tests, the specimens underwent cross-sectioning, mounting, and polishing for characterization. The corrosion behaviors of the Al/steel RSW joints were investigated using SEM. The IMCs before and after different corrosion cycles were identified using electron backscattered diffractometry (EBSD). The SEM and EBSD characterizations were carried out using the Apreo-S SEM.

To evaluate the mechanical properties of the RSW joints after different corrosion cycles, a Hysitron/Bruker PI-89 SEM Picoindenter was used for compression tests. Compared to the in-situ compression test, the in-situ compression test has a higher simplicity and ease of setup and brings an easier analysis of crack initiation and propagation. All micro-pillars were prepared using a Scios 2 DualBeam Focused Ion Beam (FIB) SEM, with a diameter of 8.2 μm and a length of 17 μm . The tests were performed at a constant strain rate of $10^{-3}/s$ in the Apreo-S SEM for in-situ imaging. Furthermore, to ensure repeatability and test accuracy, three separate micro-pillars were FIBed and compressed at the same heat input locations.

2.3. Finite element and nernst simulations

The Sorpas software [34] was used to predict the thermal and residual stress distribution at different locations of the Al/steel joints. The details of the electro-thermo-mechanical model, mechanical boundary conditions, and electro-thermal boundary conditions are presented in the previous study [32]. In addition, the major thermal and mechanical properties of the base metals (AA6022 Al alloy and HSLA340 steel) between 20 and 1200 $^{\circ}$ C were presented in the previous research [35], including density, tensile stress, yield stress, thermal conductivity, specific heat, and thermal expansion coefficient, The meshes of the 2D simulation model consisted of 1636 elements with the mesh sizes between 0.25 mm and 1 mm.

After the calculation of the thermal cycle, the temperature data of each node can be loaded into the finite element model as the thermal load to simulate the stress and train field [36]. The welding process can be simplified to a nonlinear problem of the material and the stress and strains vary linearly in a small-time increment based on the thermal load [37]. The total strain rate in the welding process is introduced as follows:

$$\mathbf{E}_{total} = \mathbf{E}_e + \mathbf{E}_p + \mathbf{E}_{th} + \mathbf{E}_{tr} + \mathbf{E}_c$$

where \mathcal{E}_{total} , \mathcal{E}_e , \mathcal{E}_p , \mathcal{E}_{th} , \mathcal{E}_{tr} , and \mathcal{E}_c are total strain, elastic strain, plastic strain, thermal strain, phase transformation strain, and creep strain,

respectively. Because of the short welding time, the creep strain and phase transformation strain can be ignored in the welding process [37]. The elastic strain and stress can be calculated by Hooke's law and the plastic strain and stress obey the VonMises criterion [38].

The Nernst equation [39] was adopted to calculate the corrosion potential under different pH values and ionic concentrations for Al, $Al_{13}Fe_4$, Al_5Fe_2 , and Fe as follows:

$$E = E^{o} - \frac{RT}{zF} ln \frac{a_{products}}{a_{reactants}}$$
 2

where E is the reversible potential of reactions, E^{o} is the standard reduction potential of reactions, $a_{products}$ is the activity of products, $a_{reactants}$ is the activity of reactants, T is the temperature in kelvin, R is the gas constant, z is the number of electrons transferred in the cathode half-cell reaction, and F is the Faraday constant.

2.4. Fracture toughness estimated by first-principles calculations

In the present study, the model by Niu et al. [40] was used to predict the fracture toughness of Al, Al₁₃Fe₄, Al₅Fe₂, and Fe,

$$K_{IC} = (1 + \alpha) \bullet V_0^{1/6} \bullet G \bullet (B/G)^{1/2}$$
 3

where K_{IC} is the fracture toughness, α is the enhancement factor calculated by the density of states at the Fermi level, $g(E_F)$, calculated by the DFT in the present work, with $\alpha=43 \bullet g(E_F)_R^{1/4}$, V_0 is volume per atom in m^3 , G is shear modulus in MPa, B is bulk modulus in MPa. For IMC of A_mB_n , the electronegativity factor, f_{EN} , is introduced for more accurate α [41]

$$\alpha = 43 \bullet g(E_F)_R^{1/4} \bullet f_{EN}$$

$$f_{EN} = \frac{\beta}{\left[1 + \frac{C_n^1 C_n^1}{C_{n+n}^2} \sqrt{\frac{(\chi_A - \chi_B)^2}{\chi_A \cdot \chi_B}}\right]^7}$$
 5

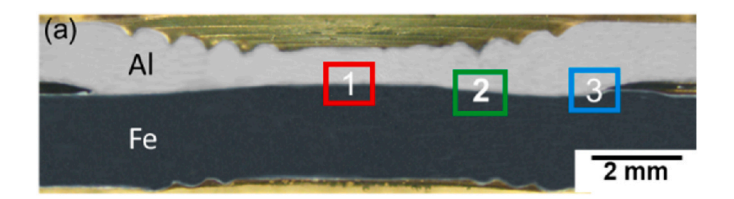
where C_m^1 , C_n^1 , and C_{m+n}^2 are the combination number for m and n in $A_m B_n$, χ_A and χ_B are the electronegativity of elements A and B in Allen scale, and β and γ are the parameters of 0.3 and 8, respectively.

In the present work, the Vienna ab initio Simulation Package (VASP) [42] was utilized for DFT-based first-principles calculations. The projector augmented wave (PAW) method was employed to describe the ion-electron interaction [43], while the exchange-correlation functional [44] was described by the generalized gradient approximation (GGA) by Perdew, Burke, and Ernzerhof (PBE). For structural relaxations and phonon calculations, a plane-wave cutoff energy of 293.2 eV was chosen, while a higher value of 520 eV was used for the final static calculations. This allowed for accurate determination of energy and electron density of states (DOS). The convergence criterion for electronic self-consistency was set to 6×10^{-5} eV/atom for structural relaxations, and static calculations. The k-point meshes (27 \times 27 \times 27), (1 \times 2 \times 2), (11 \times 6 \times 5) and (31 \times 31 \times 31) were used for relaxations and static calculations of FCC_Al, Al₁₃Fe₄, Al₅Fe₂, and BCC_Fe phases, respectively. The crystal structures of FCC_Al, Al₁₃Fe₄, and BCC_Fe were obtained from Materials Project [45], while the crystal structure of Al₅Fe₂ was generated by USPEX [46]. In the present DFT calculations, three electrons (3s²3p¹) were considered valence electrons for Al and fourteen (3p⁶3d⁷4s¹) for Fe. Fe atoms were treated as ferromagnetic spin-polarization.

3. Results

3.1. Interfacial characterization of Al/steel joints

Fig. 1 (a) presents the cross-sectioned image of the Al/steel RSW



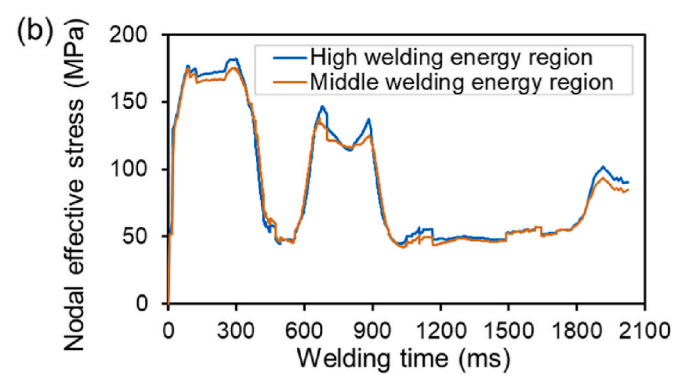


Fig. 1. (a) Macrograph of the cross-sectioned Al/steel RSW joint [32], and (b) the residual stress histories of three positions at the interface of the RSW joint.

joints before corrosion. According to the previous experimental and simulation results [32], the peak temperatures of locations 1, 2, and 3 are approximately 1150 °C, 850 °C, and 665 °C, respectively, named as the high welding energy region, the middle welding energy region, and the low welding energy region, respectively. The nodal effective residual stresses of the high and middle welding energy regions are presented in Fig. 1 (b). Due to the higher heat input and holding force from the electrodes, the region with high welding energy has a higher residual stress than the region with middle welding energy (approximately 185 MPa compared to 177 MPa).

The corrosion behavior of the Al/steel RSW joint under different corrosion cycles is illustrated in Fig. 2. Fig. 2 (a)-(c) present the SEM images of the high welding energy region before corrosion and after 7 and 26 cycles of corrosion, and Fig. 2 (d) and (e) present two different locations from the high welding energy region after 72 cycles of corrosion. With increasing corrosion cycles, severe corrosion behavior was observed. In the high welding energy region, micro-cracks initiated after 7 cycles of corrosion (Fig. 2 b), and typical pitting corrosion was observed on the Al side adjacent to the IMCs with continued corrosion (26 cycles in Figs. 2 c and 72 cycles in Fig. 2 d). Additionally, after 72 cycles of corrosion, pitting corrosion started occurring on the IMCs adjacent to steel in addition to corrosion of Al (Fig. 2 e), indicating that compared to steel, the IMC layer corrodes more easily. Fig. 2 (f)-(i) present the SEM images of the middle welding energy region after various corrosion cycles. Less corrosion was found in the middle welding energy region compared to the high welding energy region, and only several micro-cracks and pits were identified after 72 cycles of corrosion. Fig. 2 (j)-(m) present the corrosion behavior of the low welding energy region (location 3 in Fig. 1 a). Unlike the high and middle welding energy regions, which contacted the corrosion solution by micro-tunnels in the joints, the low welding energy region directly contacted the corrosion solution in the salt spray process, which resulted in more severe galvanic corrosion. As a result, pitting corrosion occurred at the Al and the IMC between Al and steel (consisting of Al, and occasional Al₅Fe₂ and Al₁₃Fe₄ grains, reported in the former study [32]) after 7 cycles of corrosion (Fig. 2 k). Steel continued to corrode after 72 cycles of corrosion (Fig. 2 m).

To evaluate the corrosion behavior of the high welding energy region, energy-dispersive X-ray spectroscopy (EDS) and EBSD methods were applied. Fig. 3 (a) and (b) present an SEM image of the high

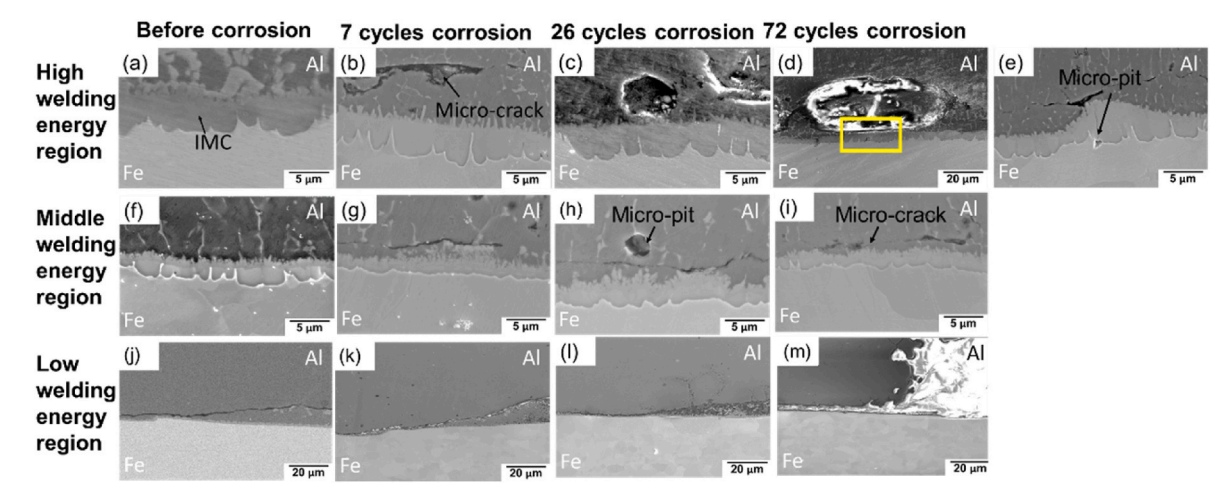


Fig. 2. Microstructures of different welding energy regions before corrosion and after 7, 26, and 72 corrosion cycles: (a)–(e) high welding energy region; (f)–(i) middle welding energy region, and (j)–(m) low welding energy region.

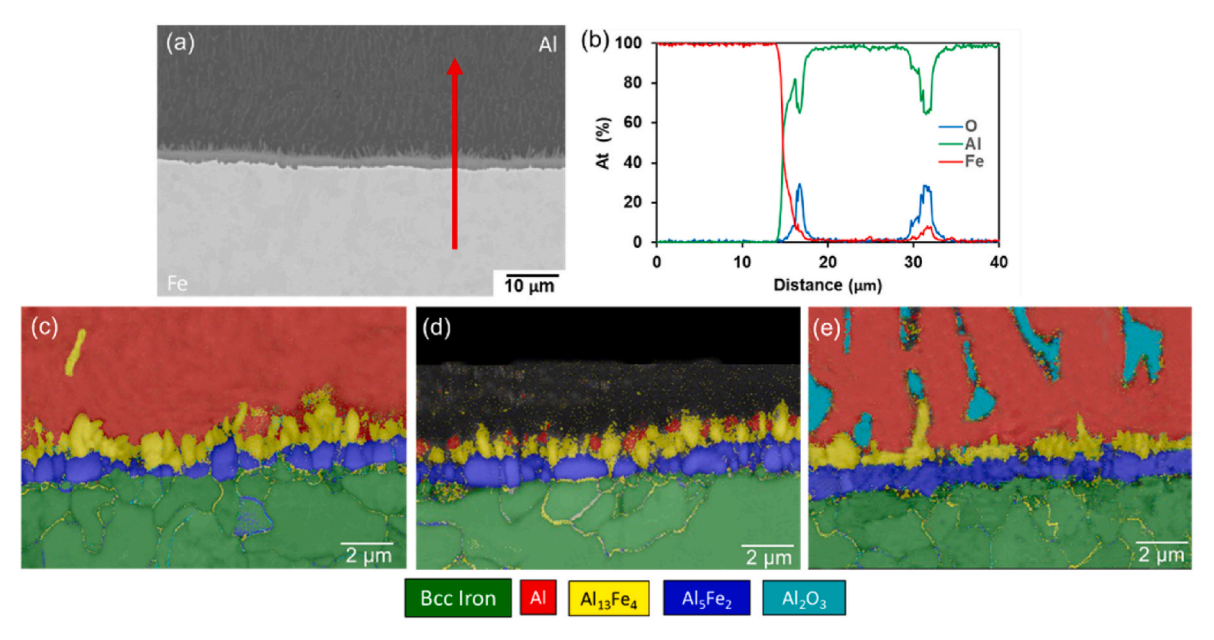


Fig. 3. (a) High welding energy region without pitting corrosion, (b) EDS line scan of the red arrow from (a), (c) EBSD of high welding energy region before corrosion, (d) EBSD of high welding energy region where Al is corroded (yellow box from Fig. 2 d), and (e) EBSD of high welding energy region with high O concentration after 72 cycles of corrosion. (For interpretation of the references to colour in this figure legend, the reader is referred to the Web version of this article.)

welding energy region and the EDS line scan results of the image, respectively. The peaks of the O element were identified on the Al side, which indicates the oxidation of Al grains. The presence of the Fe peak can be attributed to the Al₁₃Fe₄ grains within the Al matrix, as proved in our prior study [32]. Fig. 3 (c) presents the EBSD results of the high welding energy region before corrosion, and Fig. 3 (d) and (e) present the EBSD results of regions with pitting corrosion (yellow box in Fig. 2 d) and without pitting corrosion (Fig. 3 a) after 72 cycles of corrosion, respectively. According to Fig. 3 (c), after the welding process, the welding joints exhibited excellent quality, with no observable micro-holes or micro-cracks, which indicates that the emergence of micro-holes and micro-cracks is solely attributed to the effects of the corrosion. In the pitting corrosion region, compared to the IMCs before corrosion (Fig. 3 c), the Al adjacent to the IMCs was corroded after 72 cycles of corrosion. However, the Al₁₃Fe₄ particles and steel were not affected by the corrosion, indicating that Al is more susceptible to corrosion than Al₁₃Fe₄ and steel. While in the region without pitting corrosion, the product of Al after oxidation was identified as Al₂O₃ based

on the EBSD in Fig. 3 (e).

3.2. Pillar compression of Al/steel RSW joint

Mechanical properties of the Al/steel RSW joint were determined by micropillar compression. Table 2 presents the yield stress of micropillars from various welding energy regions and Fig. 4 (a) shows the average yield stress of the micro-pillars from the high and middle welding energy regions. It is observed that the compression stress of the high welding energy region is significantly higher than that of the middle welding energy region. This is because the micropillars from the high welding energy region have a thicker IMC layer than the middle welding energy region (with an average of 2.56 μm vs. 1.93 μm , calculated from the surface of the pillars before compression). The Al₅Fe₂ and Al₁₃Fe₄ phases have low ductility and high hardness (~12.79 GPa and 11.74 GPa, respectively, calculated in the former study [32]), which contributes to a high compression stress at the Al/steel joint [32,47,48]. After 72 corrosion cycles, the average yield stress of the

Table 2Yield stress of micro-pillars from various welding energy regions.

Yield stress	Test	High welding energy region	Middle welding energy region
No corrosion	test1	1101 MPa	817 MPa
	test2	1156 MPa	874 MPa
	test3	1229 MPa	830 MPa
7 cycles of	test1	1093 MPa	904 MPa
corrosion	test2	1038 MPa	855 MPa
	test3	1066 MPa	774 MPa
26 cycles of	test1	976 MPa	969 MPa
corrosion	test2	1109 MPa	918 MPa
	test3	990 MPa	918 MPa
72 cycles of	test1	740 MPa	920 MPa
corrosion	test2	942 MPa	803 MPa
	test3	1054 MPa	932 MPa

micropillars from the high welding energy region decreases from 1161 MPa to 912 MPa. Therefore, the observed galvanized corrosion on Al and IMC from Fig. 2 (d) and (e) is detrimental to the compression mechanical properties of the pillars. It should be noted that the variation in yield stresses after 72 cycles of corrosion (± 175 MPa) is relatively higher compared to those of the pillars before corrosion (± 68 MPa) and after 26 cycles of corrosion (± 75 MPa). This is due to the uneven localized corrosion after the accelerated corrosion, as shown in Fig. 4 (b)–(d). On the contrary, the average yield stress for pillars from the middle welding energy region changes from 840 MPa to 885 MPa after the 72-cycle accelerated corrosion test, which indicates that the compression mechanical properties of the pillars from the middle welding energy region are similar after corrosion. Therefore, the micro-pits and micro-cracks presented in Fig. 2 (h) and (i) have a minor influence on the yield stress of the pillars.

3.3. Crack initiation and propagation in the pillar compression of Al/steel joint

To investigate the crack initiation and propagation of the Al/steel RSW joint, the in-situ compression test was performed in the SEM to observe the deformation behavior of the micro-pillars under different corrosion and welding heat input conditions.

3.3.1. High welding energy region

Fig. 5 (a) shows the engineering stress vs engineering strain curves of the pillars from the high welding energy region before corrosion in the compression test. The pillars have an average yield stress of 1162 MPa. Stress drops were observed in test2 and test3 (green and red lines in Fig. 5 a). The stress drop is explained as a competition of relaxation from compression stress and dilatation in the shear band from shear stress [49]. The upper point of the stress drop can be explained as the dilatation resistance against shear transformation, while the lower point can be explained as shear band densification under compression and the ability to sustain reloading [50]. Jiang et al. [51] and Azadehranjbar et al. [52] discussed that brittle materials present in the pillars

significantly affect both tensile and compression mechanical properties and the stability of micropillars, such as the IMCs in this study. For the micropillars from the high welding energy region, the fraction of the IMC layer is 31.2% of the diameter of the micropillar (2.56 $\mu m/8.2~\mu m)$. Fig. 5 (b)–(e) show the SEM images of the pillar captured during the compression test (green line for test2), and Fig. 5 (f) displays the EDS mapping of the pillar after compression. Based on the SEM images of the deformed pillars, the crack initiated in the IMC at the engineering strain of 4.60% and turned into a large shear serration after 6.06% engineering strain. As the stress from the indenter increased (as seen in Fig. 5 a), the engineering stress reached about 1250 MPa, and the crack continued running across the entire pillar. Fig. 6 (a)-(c) present the cross-sectional images of the micropillar from test2 after compression, where multiple cracks were observed in the IMC layer (as seen in red boxes).

Fig. 7 (a) shows the engineering stress vs. engineering strain curves of the pillars from the high welding energy region after 26 cycles of corrosion. The average yield stress of the three pillars is 1024 MPa. Similar to the pillars before corrosion, an elastic deformation stage was observed before the yielding process. However, compared to the pillars from Fig. 5 (a), the engineering stress vs. engineering strain curves after 26 cycles of corrosion are also dominated by more frequent and larger stress drops (>50 MPa), which indicates that the deformation of the micropillars is more unstable after corrosion. Fig. 7 (b)-(e) show the SEM images of the pillar under compression test corresponding to the green line (test2) after 26 cycles of corrosion, and Fig. 7 (f) presents the EDS mapping of the pillar after compression. Localized pitting corrosion was observed in the Al phase adjacent to the IMC layer (see Fig. 7 b), which matches the SEM image in Fig. 2 (c). At the same time, slight pillar widening can be observed (Fig. 7 c). From the recorded SEM images, deformation instability (the non-uniformity and unstable deformation of materials under loading conditions, mentioned by Wan et al. [53]) was initiated at the micro-cracks and micro-pits in the Al matrix next to the IMC layer (Fig. 7 d and f) and spread along the interface between Al and IMC layer through the entire pillar (Fig. 7 e). Fig. 6 (d)-(f) show the cross-sectional images of the micropillar from test2 after compression. In addition to the primary crack (red arrow in Fig. 7 d) that originated from the Al matrix, a micro-crack was also observed in the IMC layer (red box in Fig. 6 d). A similar phenomenon also was seen in the pillar before corrosion (Fig. 6 a-c). The crack prefers to initiate at the Al₅Fe₂ phase and propagate near the 45° direction. Therefore, the failure of the pillars after 26 cycles of corrosion is attributed to a combination of pitting corrosion of the Al matrix and brittle fracture of the IMC phase.

Fig. 8 (a) displays the engineering stress vs. engineering strain curves of micropillars from the high welding energy region after 72 cycles of corrosion. The yield stress of the three tests is 740 MPa, 942 MPa, and 1054 MPa, respectively (mentioned in Section 3.2). Small stress drops (≤50 MPa) were observed before yielding. The occurrence of deformation instabilities under relatively low strains suggests that corrosion significantly affects the deformation morphology of the Al-IMC-steel structure. Fig. 8 (b)−(f) display the SEM images and EDS results distribution from the high welding energy region after 72 cycles of corrosion. In this case, most of the Al phase adjacent to the IMC has been corroded

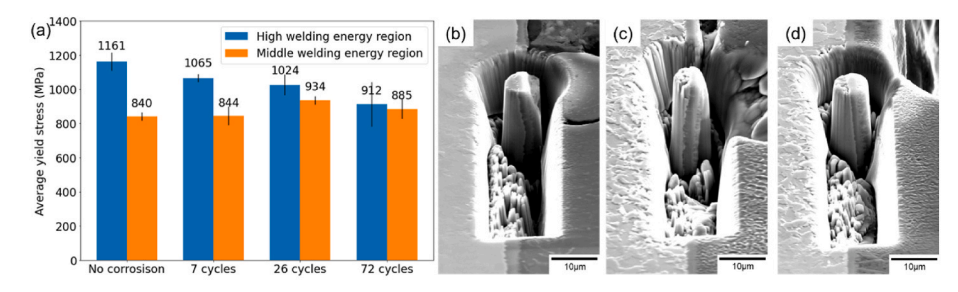
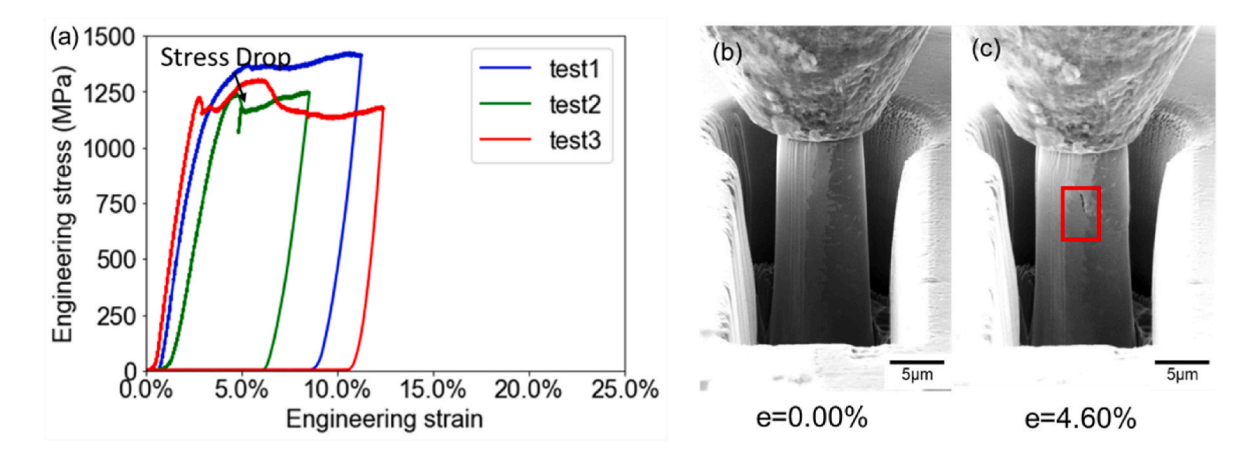


Fig. 4. (a) Average yield stress of high and middle welding energy regions under different corrosion conditions, (b)–(d) pillars from high welding energy region after 72 cycles of corrosion.



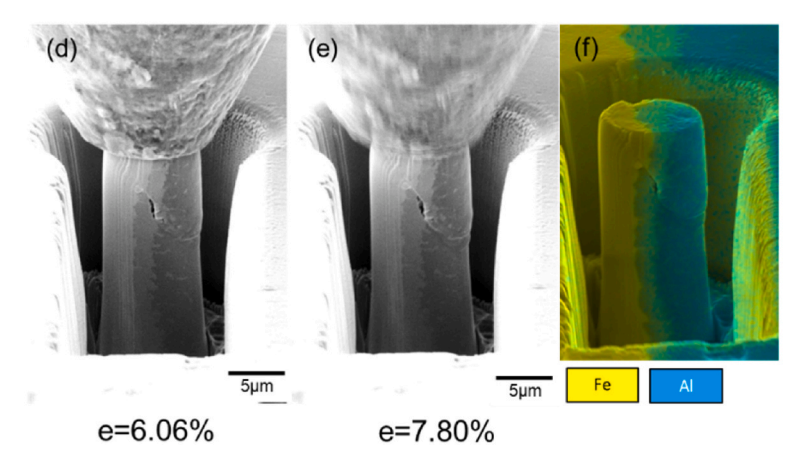


Fig. 5. (a) Stress-strain curve of micropillars before corrosion, (b)-(e) SEM images of micro-pillars from test2, and (f) EDS of the micropillar after compression.

(Fig. 8 f), and the compression force was directly applied to the IMC and steel. Apart from the failure in the IMC and Al phase, a new failure mode was observed in the micropillars after 72 cycles of corrosion in addition to the fracture at the Al/IMC interface. Due to localized corrosion on Al $_5$ Fe $_2$ at the interface of IMC/steel, the micro-cracks originated at the IMC/steel interface when the engineering strain reached 3.09% (as seen in Fig. 8 c). Consequently, the cracks propagated into the Al $_5$ Fe $_2$ in the IMC layer near the 45° direction in the continuous plastic deformation. It should be noted that the failure of pillars after 72 cycles of corrosion is due to multiple crack propagation (as seen in Fig. 6 g and h). The microcracks were generated from different pitting corrosion locations and propagated into the IMC layer of the micropillar.

$3.3.2. \ \ \textit{Middle welding energy region under different corrosion conditions}$

Fig. 9 (a) presents engineering stress vs. engineering strain curves of the micropillars from the middle welding energy region before corrosion in the compression test. All three pillars present similar mechanical properties and deformation behavior with an average yield stress of about 840 MPa. Fig. 9 (b)–(e) show the compression process of the pillar from test3, and Fig. 9 (f) presents the EDS mapping of the pillar. Initially, elastic deformation was observed, followed by plastic deformation, and the primary micro-crack was generated when the engineering strain reached 8.58 % (Fig. 9 c). Subsequently, the micro-cracks propagated in the IMC layer along about 45° direction (explained in Section 4.2.1), and shear steps appeared on the surface of the pillar. Subsequently, deformation advanced, and the crack persisted in its propagation into the steel phase, similar to the deformation of the pillar from the high welding energy region. (Fig. 5). It is noteworthy that the direction of shear steps in the Al is not the same as those of the IMC and steel, but

rather symmetric (white and red arrows in Fig. 9 d). After the failure of IMC and steel, the applied compression stress on the surface of the pillar is uneven. Under this condition, the secondary crack originated from the tip of the primary crack and propagated in the Al phase near the 45° direction (Fig. 9 e). Comparing the engineering stress vs. engineering strain curves of the pillars from the high and middle welding energy regions, the pillars from the middle welding energy region have lower yield stress but higher ductility due to the thinner IMC layer in the pillars (as mentioned in Section 3.2). Meanwhile, large stress drops were not observed in the stress-strain curves of the pillars, indicating that the middle welding energy region with the thinner IMC layer has a higher initial activation energy for shear transformation compared to the high welding energy region.

Fig. 10 (a) displays the engineering stress vs. engineering strain curves of the micropillars from the middle welding energy region after 72 cycles of corrosion. The average yield stress is 865 MPa and the pillars from tests 1 and 2 exhibited a similar deformation behavior to the pillars before corrosion. This is attributed to the less corrosion that occurred in joints prepared in the middle welding energy region. However, for test3, a large stress drop was observed on the stress-strain curve, indicating that micro-cracks and micro-pits after corrosion can affect the deformation behavior of the micropillar with the Al-IMC-steel structure. Fig. 10 (b)-(e) present the SEM images of the failure of the pillar from test3 and Fig. 10 (f) displays the EDS mapping of the pillar after compression. Two micro-cracks (red and yellow boxes in Fig. 10 b) initiated simultaneously in the IMC layer of the pillar at the engineering strain of 6.29%, which contributes to the complicated formation and movement of shear steps in the Al₅Fe₂ grains. Consequently, with the continued deformation development, the two micro-cracks gradually

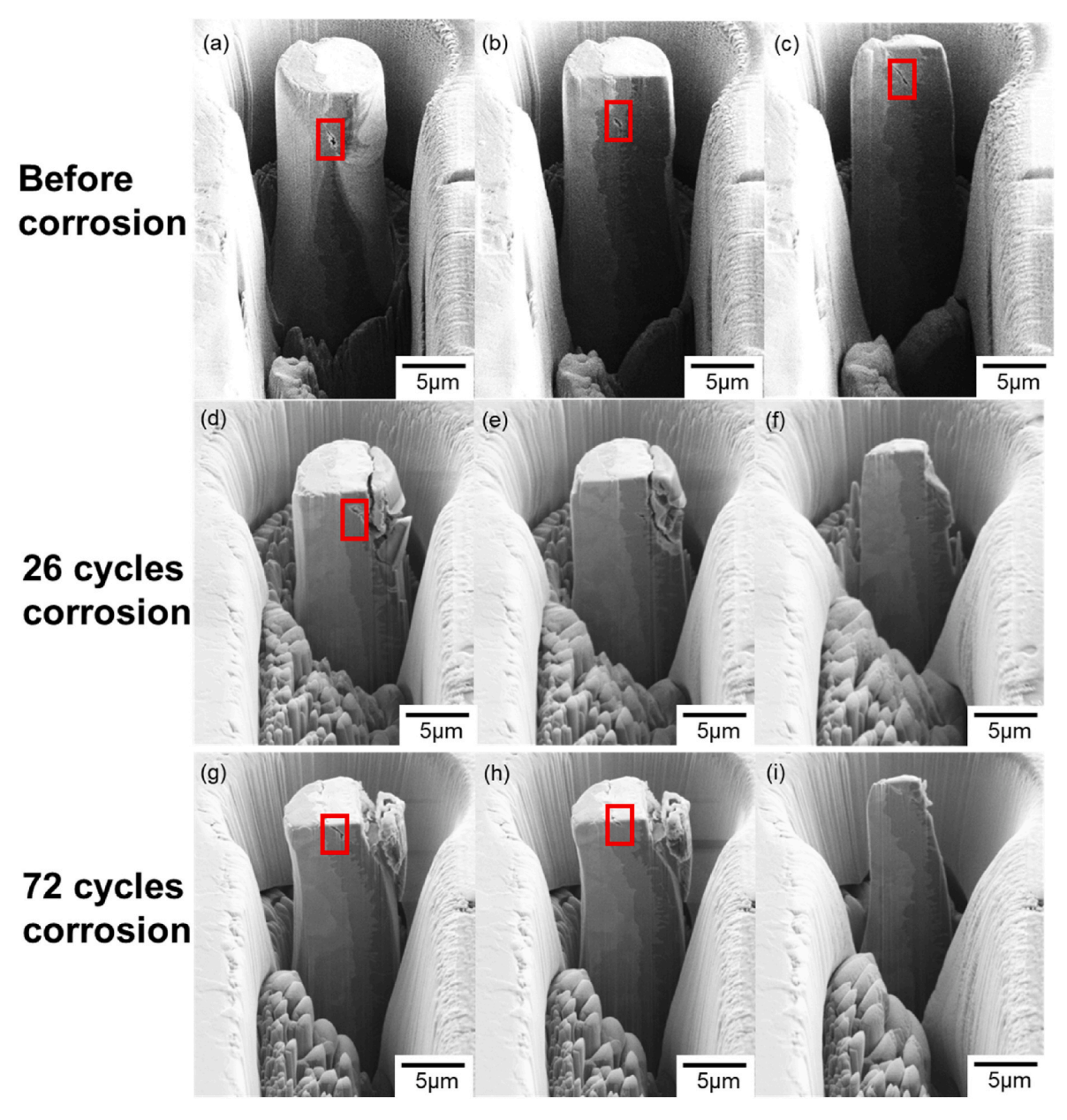


Fig. 6. Cross-sectioned images of micropillars under various corrosion cycles: (a)-(c) before corrosion, (d)-(f) 26 cycles, and (g)-(i) 72 cycles.

propagated into the steel and Al (red and white arrows in Fig. $10\,$ e), respectively.

4. Discussion

4.1. Corrosion mechanism of the Al/steel joints

Fig. 11 (a)-(c) depict the proposed corrosion mechanism of the high welding energy region under different corrosion conditions. As the number of corrosion cycles increases, localized corrosion occurs gradually at the interface of the Al/steel joints. Although the high and middle welding energy regions don't have direct contact with the corrosion solution in the crevice of the Al/steel RSW joint, these regions can face the corrosion solution by the defects (like micro-channels) in the welding process.

Pitting corrosion was observed on the Al adjacent to the IMC layer after 26 cycles of corrosion (Fig. 11 b). Based on the Nernst equation and the present DFT calculations, the corrosion potentials of Al, $Al_{13}Fe_4$, Al_5Fe_2 , and Fe are 5.40–5.68 V, 4.34–4.62 V, 4.10–4.38 V, 1.69–1.97 V

from pH values of 6.1-6.5, respectively [54]. As mentioned in Section 2.1, the pH value of the corrosion solution is 6.1–6.5 [12]. Under this condition, Al serves as the anode, and long needle-like Al₁₃Fe₄ (with corrosion potential 4.10-4.38 V from pH 6.1-6.5) serves as the cathode, leading to minimal corrosion in the Al matrix. It should be noted that a large amount of Fe atoms diffuses into the Al matrix due to the RSW process, which reacts with the Al atoms and generates the short needle-like Al₁₃Fe₄ phase in the Al matrix [13,15,32]. Therefore, minimal corrosion also occurred at the Al matrix adjacent to the short needle-like Al₁₃Fe₄, resulting in enhanced corrosion of Al [55]. After 72 cycles of corrosion (Fig. 11 c), severe corrosion was observed at the Al matrix with the accumulation of minimal corrosion, and a continuous corrosion crack was observed at the interface of Al/IMC (Fig. 2 d). At the same time, minimal corrosion occurred at the Al₅Fe₂ because Al₅Fe₂ is less noble than Fe (Fig. 11 c). Al₅Fe₂ serves as the anode, contributing to the dissolution of the Al₅Fe₂ adjacent to the steel/IMC layer (Fig. 2 e). Compared to the galvanic corrosion of Al, the corrosion rate of Al₅Fe₂ remains at a lower level.

Less severe corrosion was observed in the middle welding energy

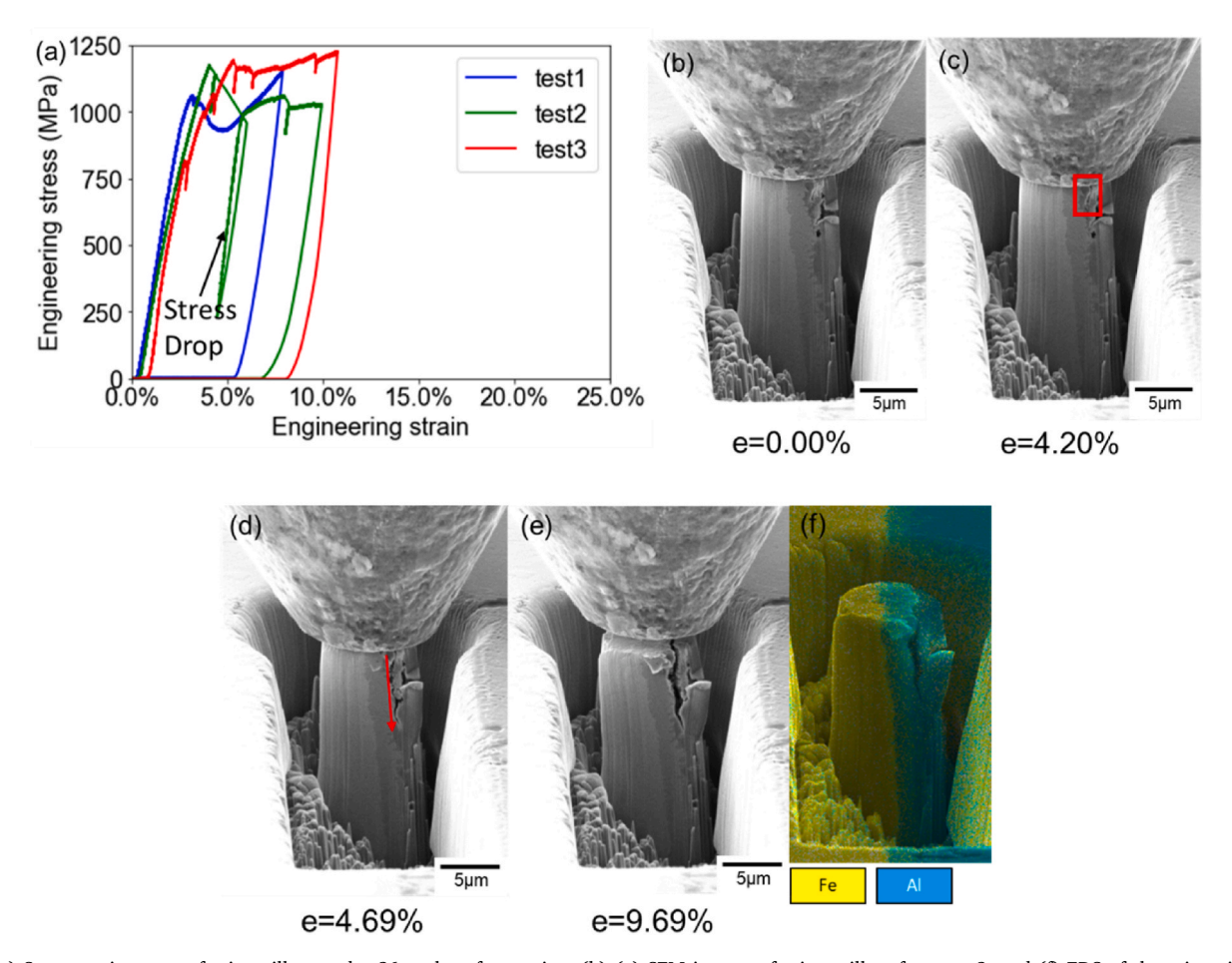


Fig. 7. (a) Stress-strain curve of micropillars under 26 cycles of corrosion, (b)–(e) SEM images of micro-pillars from test2, and (f) EDS of the micropillar after compression.

region compared to the high welding energy region. Compared to the large area pitting corrosion in the high welding energy region, only micro-cracks and pits were observed in the middle welding energy region after 72 cycles of corrosion, similar to Fig. 11 (b). According to Mansfeld [56], the galvanic corrosion rate is directly influenced by the ratio of anode and cathode area:

$$I_g = I_L \bullet (A_{cathode} / A_{anode})$$

where I_g is the galvanic current, I_L is the limited diffusion current density, and Acathode and Aanode are the areas of the cathode and anode regions, respectively. For the corrosion performance on the interfacial layer, the diffusion current densities between Al and Al₁₃Fe₄ are equal at the high and middle welding energy regions, because of the same types of IMC phases at these two regions (proved in the former study [32]). Therefore, the galvanic current is directly affected by the ratio of the cathode and anode areas. Compared to the middle welding energy region, the thickness of the IMC layer in the high welding energy region is larger (2.56 μm vs. 1.93 μm , from Section 3.2). At the same time, the higher energy input in the high welding energy region also increases the diffusion rate of Fe atoms in the Al matrix $(10^{-7.87} \text{ m}^2/\text{s vs. } 10^{-8.45} \text{ m}^2/\text{s})$, according to the former study [32]), leading to more IMC formed in the Al matrix (as shown in Fig. 12 a-d). The IMC phase has been proved as $Al_{13}Fe_4$ in the former study [32]. As a result, the $A_{cathnode}/A_{anode}$ value in the high welding energy region is considerably greater than that in the middle welding energy region, resulting in a stronger galvanic current between the Al and Al₁₃Fe₄ phases and a higher corrosion rate on the Al matrix. Additionally, the higher residual stress in the high welding energy region (shown in Fig. 1 b) also exacerbates the corrosion of Al. According to Dong et al. [57] and Ming et al. [58], residual stress increased stress corrosion cracking (SCC) susceptibility and SCC growth rates in the welding zone. SCC prefers to propagate along regions with high residual stress concentration, high corrosion potential, high micro-hardness, and high-angle grain boundaries [59]. Therefore, due to the higher galvanic current and residual stress, the Al matrix in the high welding energy region has a lower corrosion resistance than the middle welding energy region, which contributes to the severe corrosion occurring in the high welding energy region.

4.2. Fracture mechanism of micropillars in compression test under different corrosion conditions

According to the crack initiation and propagation of pillars from Section 3.3, the fracture mechanism of the pillars is summarized in Fig. 13.

4.2.1. Fracture mechanism before corrosion or under the minimal corrosion condition

Fig. 13 (a) shows the fracture mechanism of the pillars before corrosion or under minimal corrosion conditions, which presents the pillars from the high welding energy region before corrosion and the middle welding energy region after 0–72 cycles of corrosion. In this condition, the IMC layer is not corroded, and the Al matrix is barely corroded. Micro-cracks are initiated at different locations in the IMC layer of the micropillar (Fig. 6 a-c). Using Niu et al.'s model [30], the predicted $K_{\rm IC}$ values of Al, $Al_{13}Fe_4$, Al_5Fe_2 , and Fe in comparison with experimental values as summarized in Table 3, with the Al_5Fe_2 phase exhibiting the lowest value. According to experiments by Windmann et al. [60] in terms of Laugier's equation [61], the estimated $K_{\rm IC}$ values

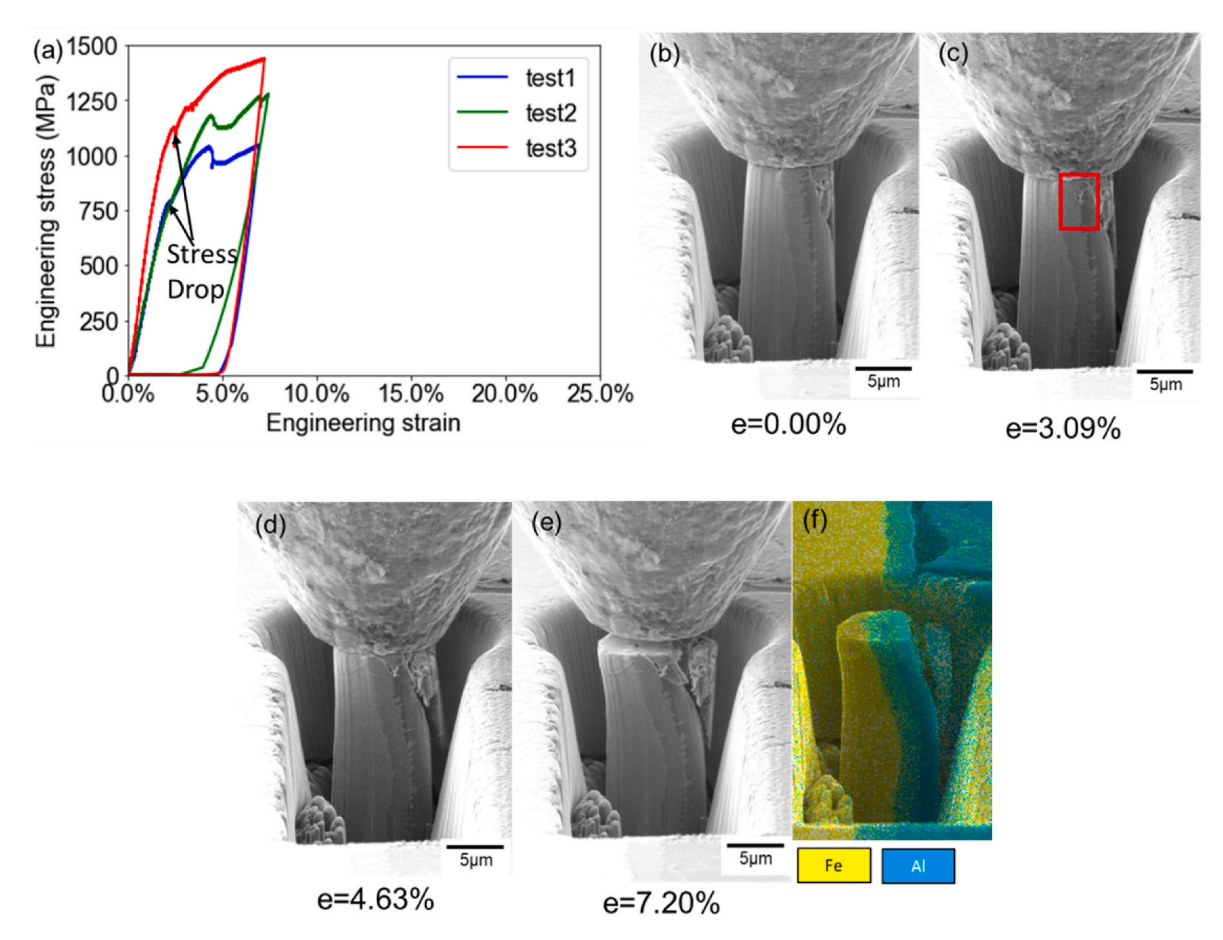


Fig. 8. (a) Stress-strain curve of micropillars under 72 cycles of corrosion, (b)–(e) SEM images of micro-pillars from test1, and (f) EDS of the micropillar after compression.

are 1.4 and 0.9 MPa \sqrt{m} for Al₁₃Fe₄ and Al₅Fe₂, respectively. The K_{IC} values of pure elements such as Al (29.1 MPa \sqrt{m}) and Fe (112.4 MPa \sqrt{m}) were found to be less than 8% different from experimental data summarized in paper of Niu et al. [41], which reported the K_{IC} values of 30–35 MPa \sqrt{m} for Al and 120–140 MPa \sqrt{m} for Fe. The experimental K_{IC} values of $Al_{13}Fe_4$ and Al_5Fe_2 are 1.4 MPa \sqrt{m} and 0.9 MPa \sqrt{m} , respectively, while the predicted K_{IC} values of $Al_{13}Fe_4$ and Al_5F_{e2} are 24.0 MPa \sqrt{m} and 15.0 MPa \sqrt{m} , respectively. The reason for the difference between the experimental and predicted K_{IC} values is the high error on K_{IC} values calculation based on the indentation fracture test using Laugier's equation [62]. However, these are the only available K_{IC} values of Al₁₃Fe₄ and Al₅Fe₂ from the experimental test. The computational predictions indicate a trend of Fe > Al > Al₁₃Fe₄ > Al₅Fe₂, which aligns well with the observed trend based on experimental data. Therefore, IMCs such as Al₁₃Fe₄ and Al₅Fe₂ demonstrate significantly lower K_{IC} values compared to pure elements. This is primarily due to their ordered crystal structures, which limit their ability to undergo plastic deformation as they possess fewer slip systems.

In the plastic deformation of the pillars, the observed shearing can be observed on the micropillars with the Al-IMC-steel "sandwich" structure. The shear steps are apparent on the pillar surface, and the shear bands initiate from the Al_5Fe_2 phase (see Fig. 5 b and f). Based on the stress analysis on the tip of the micro-crack in the Al_5Fe_2 phase, there are two possible directions for crack propagation, i.e., 0° along the direction of principal compression stress and 45° along the direction of the maximum shear stress. Based on the results from Beygi et al. [63], when the load is applied on the interface of dissimilar material joint, the shear stress has a significant influence on the fracture behavior of the joints. According to Chen et al. [13], in the absence of diminished interfacial

fracture toughness due to grain coursing, the thin IMC layer has relatively high resistance for crack propagation in the IMC parallel to the interface, so the cracks prefer to propagate along the shear stress direction approach Al and steel side and form the primary crack [64]. Ultimately, the cracks cross the interface of Al/IMC and IMC/steel under the shear direction (black arrows in Fig. 13 a) and result in the fracture of the whole pillar. The fracture at the interface of the Al/steel joint occurs in a brittle manner under shear loading conditions, ultimately contributing to the failure observed at the IMC layer [63]. This fracture mechanism is applied to the pillars from the high welding energy region before corrosion (Fig. 5) and the middle welding energy region before and after corrosion. However, the difference on the deformation morphology between pillars from the high and middle welding energy should also be mentioned. Compared to the pillars from the middle welding energy region, pillars from the high welding energy region have more hard and brittle IMCs (proved by the former study [32] and Chen et al. [13]), which contributes to a lower K_{IC} for the Al-IMC-steel structure in the pillars (based on Table 3). Therefore, the pillars from the high welding energy region have lower resistance for crack initiation and propagation [13,47,65], leading to the formation of deformation stability at an earlier engineering strain (4.60% vs. 5.58% from Figs. 5 c and Fig. 9 c, respectively).

4.2.2. Fracture mechanism under the moderate corrosion condition

Fig. 13 (b) presents the fracture mechanism of the pillars under the moderate corrosion condition, which counts for the pillars from the high welding energy region after 26 cycles of corrosion. Localized galvanic corrosion is generated at the Al phase adjacent to the needle-like $Al_{13}Fe_4$ phase. Simultaneously, while the IMC phases are not corroded. Under this condition, in addition to the initiation of new cracks in the IMC

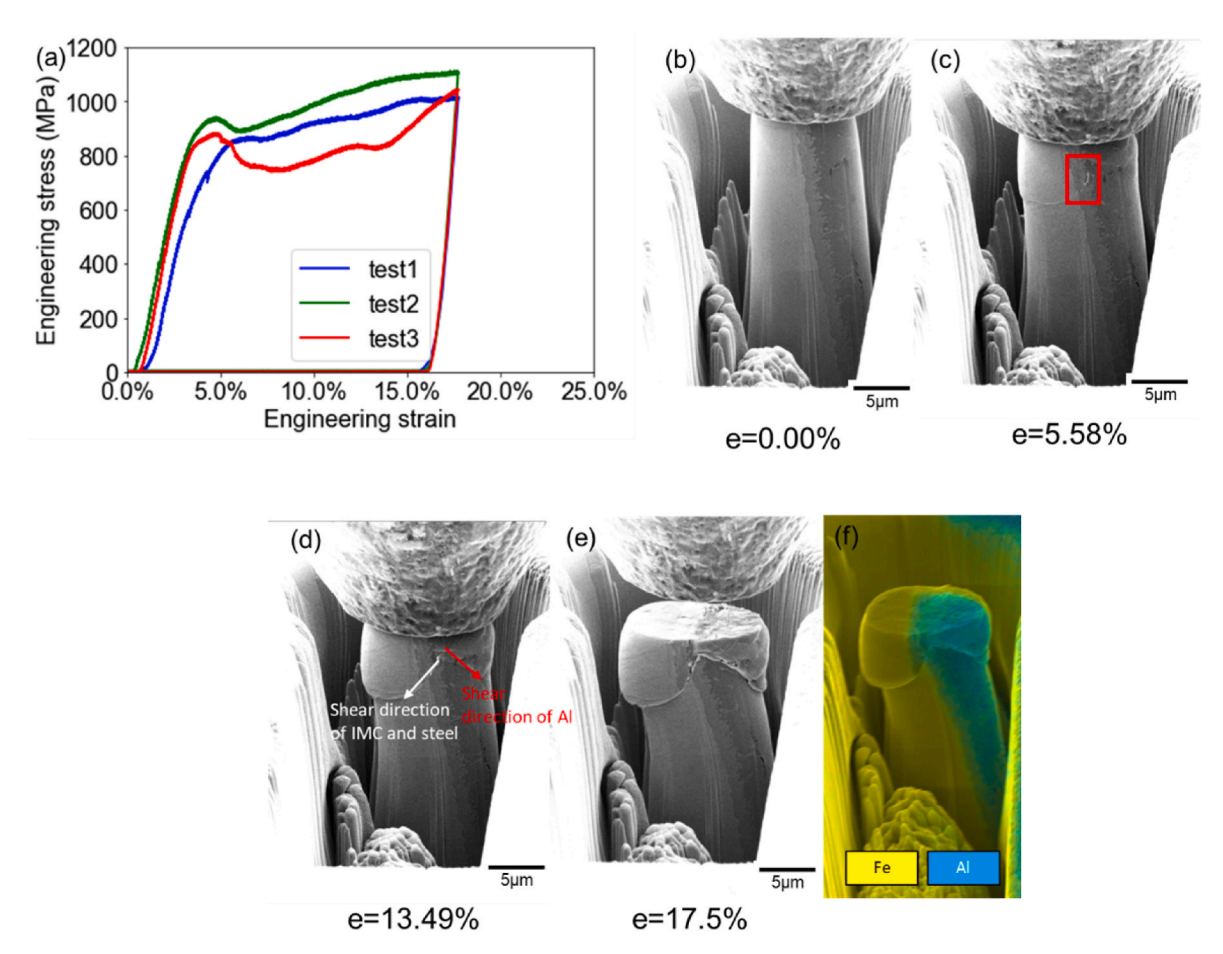


Fig. 9. (a) Stress-strain curve of micropillars before corrosion, (b)-(e) SEM images of micro-pillars from test3, and (f) EDS of the micropillar after compression.

layer, the micro-cracks and pits formed in the corrosion process can directly propagate along the interface of Al/IMC (the black arrows in Fig. 13 b) and result in the failure of the pillar. This can be attributed to three reasons: (1) micro-cracks and pits formed along the IMC/Al interface during corrosion; (2) defects generated during the welding process, such as vacancies [66]; and (3) high residual stress at the boundary of the IMC/Al interface. The presence of tensile residual stress functions as a preliminary tensile procedure, augmenting the propagation of micro-cracks. The tensile residual stress acts as a pre-tensile process and promotes micro-crack propagation [67]. The accumulation of multiple micro-cracks propagation at the interface of Al/IMC and the compression load from the normal direction leads to the failure of the pillar [63]. Compared to the IMC layer, the micro-cracks and micro-pits formed after corrosion have lower structural resistance to shear deformation, which leads to frequent stress drops in the compression process (Fig. 7a). As a result, the cracks propagate along the Al/IMC interface under lower loads than those in the absence of corrosion, leading to the lower yield stress of the micropillars (Fig. 4 a). Because of the corrosion occurred on the Al matrix, fractures will occur at the interface of Al/IMC in the macro-scale lap-shear test, which will be discussed in detail in our future study.

4.2.3. Fracture mechanism under the severe corrosion condition

The fracture mechanism of the micropillars under the severe corrosion condition is depicted in Fig. 13 (c), which counts for some pillars from the high welding energy region after 72 cycles of corrosion (like the pillar in Fig. 8). In this case, the failure of the pillars is due to a combination of the fracture at the Al/IMC interface and the fracture in the IMC layer. The fracture at the Al/IMC interface results from the microcracks and micro-pits propagation along the Al/IMC interface, as

introduced in Section 4.2.2. The fracture in the IMC is based on the localized galvanic corrosion that occurs on the Al₅Fe₂ (Fig. 11 c) of pillars from the high welding energy region after 72 cycles of corrosion. As presented in Fig. 8 (b)–(e), the micro-cracks initiate at the interface of IMC/steel. This can be attributed to the micro-cracks and micro-pits generated after the galvanic corrosion of Al₅Fe₂, as well as the high residual stress between the IMC and steel induced during the welding process (as seen in Fig. 1 b) [68,69]. It should mention that only a limited number of micro-pits were observed at the Al₅Fe₂/Fe interface, a phenomenon attributed to the inhibitory effect of galvanic corrosion in the aluminum. This inhibition of corrosion on the IMCs leads to a comparatively low corrosion rate for the Al₅Fe₂ phase. In this scenario, instead of growing along the Al₅Fe₂/Fe interface, the micro-cracks prefer to propagate into the Al₅Fe₂ phase due to the lower K_{IC} of Al₅Fe₂ when compared to the Fe matrix. Relative to the Al matrix with micro-cracks and micro-holes, the structural resistance to shear deformation within the IMCs is higher. Therefore, the frequent large stress drops were not observed on the stress-strain curves for the pillars after 72 cycles of corrosion (Fig. 8 a). Eventually, the micro-cracks propagate along the shear direction in the Al₅Fe₂ phase, due to the low shear modulus [70]. Similar to the moderate corrosion condition, fractures are observed at the Al/IMC interface for the Al/steel RSW joints under the severe corrosion condition in the macro-scale lap-shear test, which will be investigated in our future study.

5. Conclusions

The present work comprehensively investigated the effects of welding heat input on the formation of IMCs, corrosion mechanism, and micro-crack initiation and propagation in Al/steel RSW joints. The

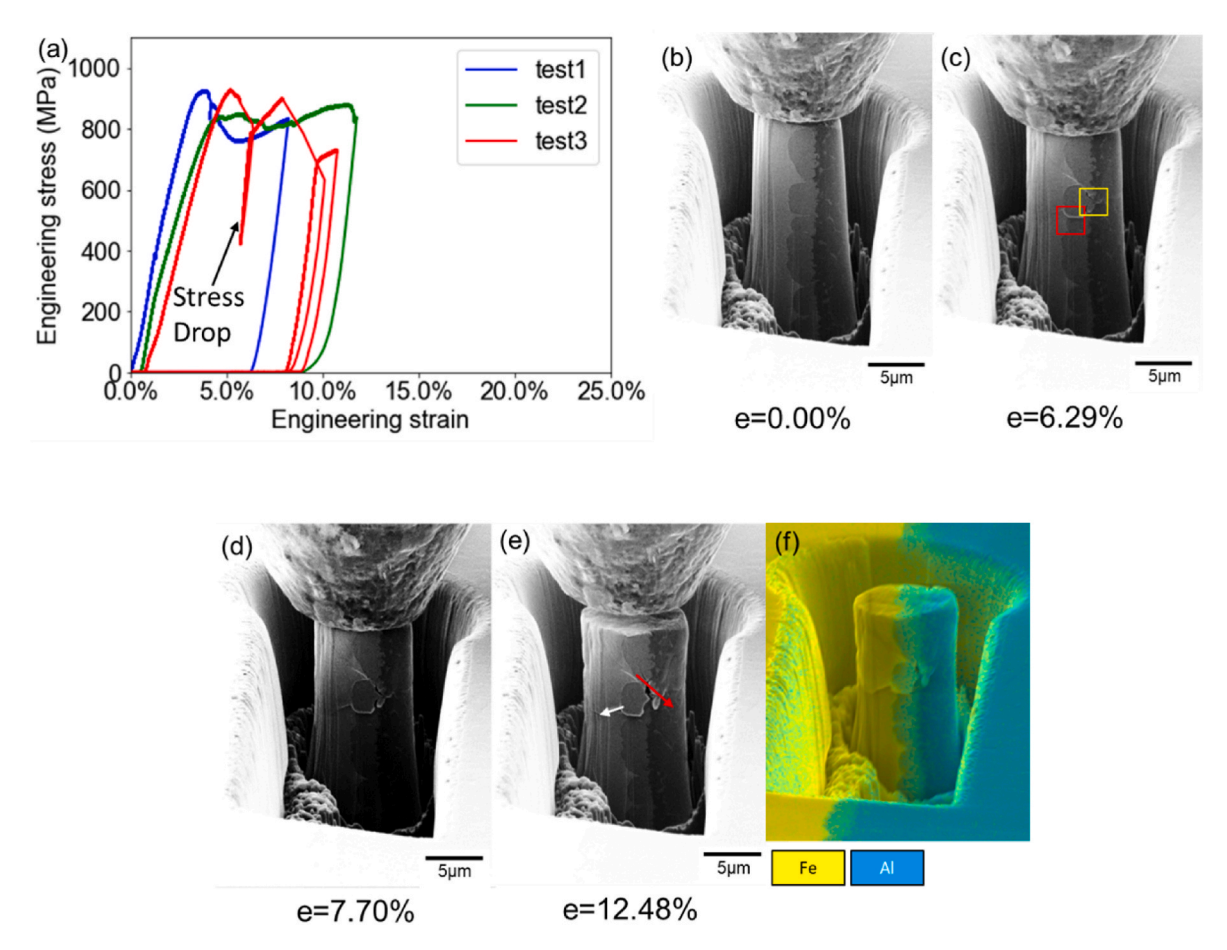


Fig. 10. (a) Stress-strain curve of micropillars under 72 cycles of corrosion, (b)–(e) SEM images of micro-pillars from test3, and (f) EDS of the micropillar after compression.

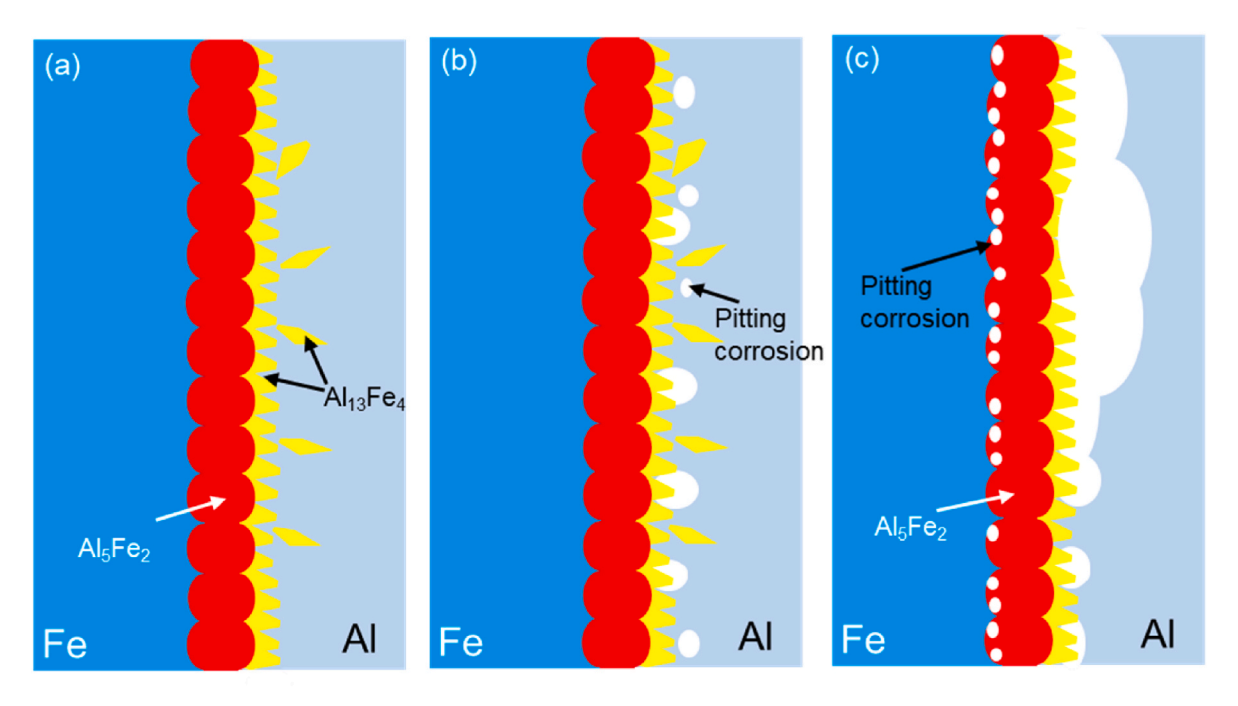


Fig. 11. Proposed corrosion mechanism of high energy region: (a) before corrosion (Fig. 3 a), (b) 26 cycles of corrosion, and (c) 72 cycles of corrosion.

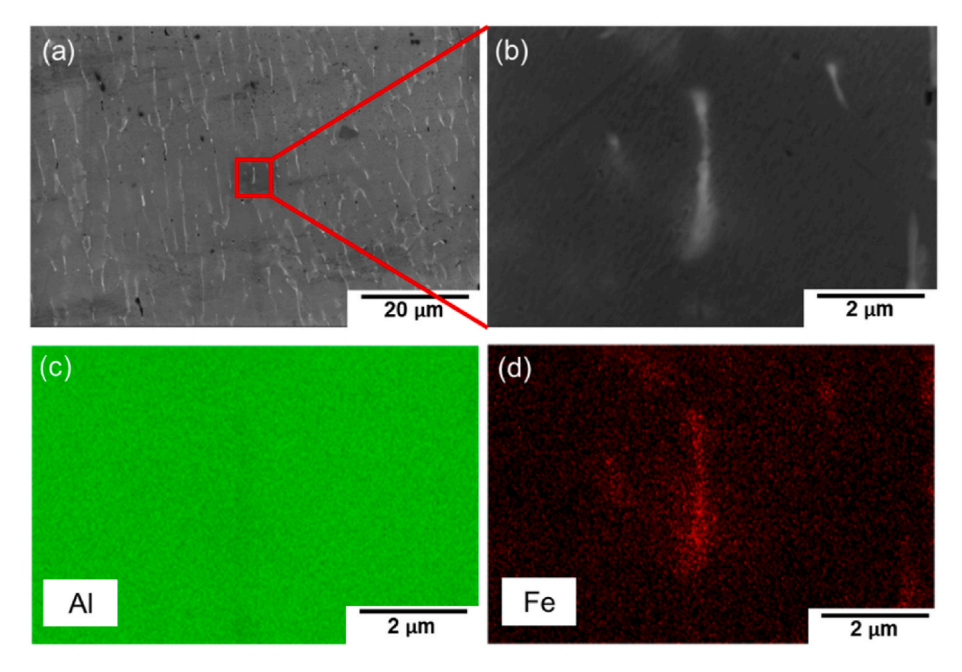


Fig. 12. (a) Al phase adjacent to IMC layer, (b) needle-like phase, (c), (d) Al and Fe element distribution in the Al matrix.

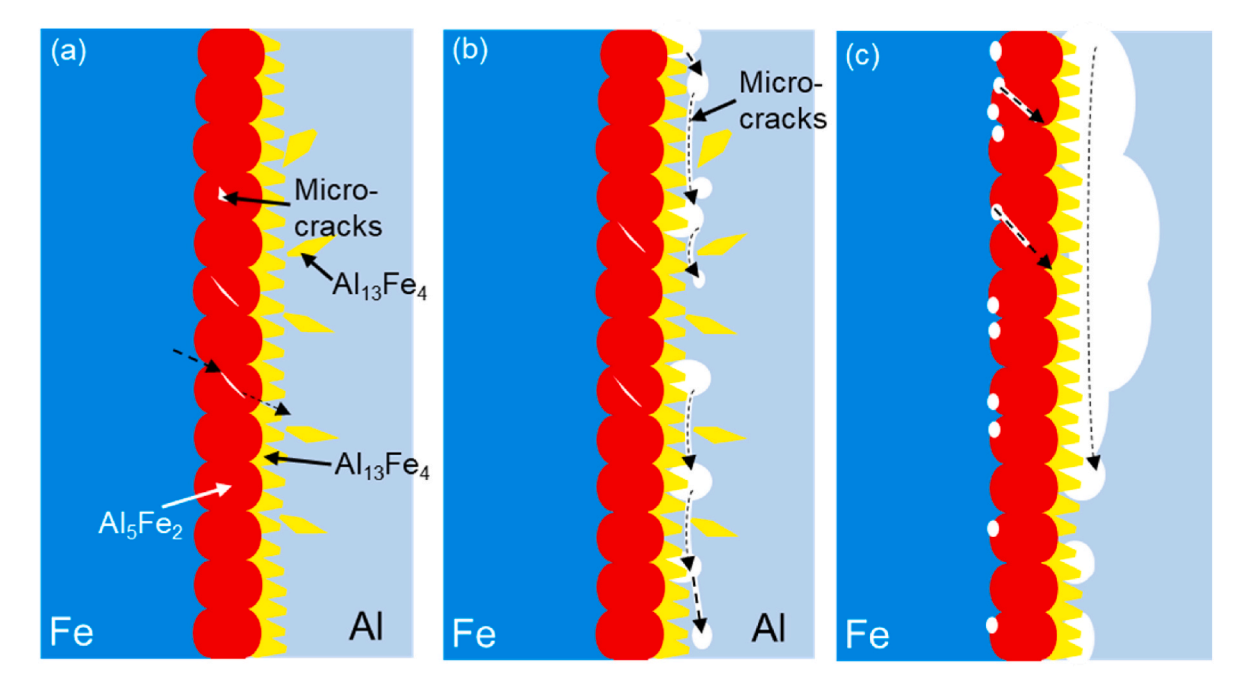


Fig. 13. Schematic of the fracture mechanism of micropillars under different (a) before corrosion or under the minimal corrosion, (b) moderate corrosion, and (c) severe corrosion conditions.

Table 3 The predicted K_{IC} values (MPa \sqrt{m}) of Al, Al $_{13}$ Fe $_4$, Al $_5$ Fe $_2$, and Fe in comparison with experimental values.

Compounds	Predicted K_{IC} values	Experimental K_{IC} data	References of experiments
Al	29.1	30–35	Niu et al. [41]
$Al_{13}Fe_4$	24.0	1.4	Windmann et al. [60]
Al ₅ Fe ₂	15.0	0.9	Windmann et al. [60]
Fe	112.4	120-140	Niu et al. [41]

corrosion potentials of Al, Fe, Al $_5$ Fe $_2$, and Al $_1$ 3Fe $_4$ were calculated by the Nernst equation. The *in-situ* compression was applied to investigate the compression mechanical properties and deformation behavior of the pillars under different heat inputs and corrosion conditions. The results are summarized in the following:

1. Galvanic corrosion first occurred at Al (next to $Al_{13}Fe_4$), then Al_5Fe_2 (adjacent to steel) in the salt spray corrosion. Corrosion potential simulations for Al, $Al_{13}Fe_4$, Al_5Fe_2 , and Fe indicated that IMC phases can cause local potential differences, leading to localized galvanic corrosion on Al and Al_5Fe_2 .

- 2. The high welding input reduced the corrosion resistance of the Al/steel RSW joint, due to the thick IMC layer and high residual stress at the interface. High welding energy promoted the formation of Al_5Fe_2 and $Al_{13}Fe_4$ at the Al/steel interface and $Al_{13}Fe_4$ in the Al matrix, which accelerated the corrosion of Al. The higher residual stress also increased the SCC susceptibility of the high welding energy region.
- 3. Compared to the middle welding energy region, corrosion had a more significant influence on the compression properties of the high welding energy region. The average yield stress of pillars from the high welding energy region decreased from 1161 MPa to 912 MPa after 72 cycles of corrosion, while the middle welding energy region is similar after corrosion.
- 4. Three crack initiation and propagation mechanisms were proposed under different conditions. The IMC phases showed significantly lower $K_{\rm IC}$ values than AA6022 and HSLA340, leading to crack initiation. Under before or minimal corrosion conditions, cracks initiated and propagated in the IMC layer in the shear direction. Under the moderate corrosion condition, cracks propagated at the Al/IMC interface. The fracture of the pillar under the severe corrosion condition was due to both cracks propagating at the Al/IMC interface and new micro-cracks initiated in the Al_5Fe_2 phase at the IMC/steel interface.

CRediT authorship contribution statement

Bo Pan: Conceptualization, Methodology, Writing – original draft, Writing – review & editing. Hui Sun: Software, Visualization, Writing – original draft, Writing – review & editing. Dongyue Xie: Investigation, Data curation. Shun-Li Shang: Formal analysis, Writing – review & editing, Supervision, Project administration. Nan Li: Supervision, Project administration. Supervision, Funding acquisition. Yumeng Li: Supervision. Zi-Kui Liu: Writing – review & editing, Supervision, Project administration, Funding acquisition. Jingjing Li: Writing – review & editing, Supervision, Project administration, Funding acquisition. Funding acquisition.

Declaration of competing interest

The authors declare that they have no known competing financial interests or personal relationships that could have appeared to influence the work reported in this paper.

Data availability

The data that has been used is confidential.

Acknowledgement

This work was performed, in part, at the Center for Integrated Nanotechnologies, an Office of Science User Facility operated for the U. S. Department of Energy (DOE) Office of Science. Los Alamos National Laboratory, an affirmative action equal opportunity employer, is managed by Triad National Security, LLC for the U.S. Department of Energy's NNSA, under contract 89233218CNA000001. The authors would like to acknowledge the support of the U.S. National Science Foundation through Civil, Mechanical, and Manufacturing Innovation Grants No. 1651024 and 2226976. Additionally, the authors express their gratitude to Dr. Pei-Chung Wang from Global Research and Development for providing FEM simulation support.

References

[1] J. Bi, L. Wu, Z. Liu, H. Wang, Q. Li, Z. Yang, Coupling effect of ultrasonic vibration and beam oscillation on FQZ soften inhibition of laser welded Al-Mg alloy joints, Mater. Lett. X 18 (2023), 100197, https://doi.org/10.1016/J. MLBLUX.2023.100197.

- [2] J. Bi, L. Wu, Z. Liu, H. Wang, Q. Li, Z. Yang, Coupling effect of ultrasonic vibration and beam oscillation on FQZ soften inhibition of laser welded Al-Mg alloy joints, Mater. Lett. X 18 (2023), 100197, https://doi.org/10.1016/J. MLBLUX.2023.100197.
- [3] P. Geng, M. Morimura, H. Ma, Y. Ma, N. Ma, H. Liu, Y. Aoki, H. Fujii, G. Qin, Elucidation of intermetallic compounds and mechanical properties of dissimilar friction stir lap welded 5052 Al alloy and DP590 steel, J. Alloys Compd. 906 (2022), 164381, https://doi.org/10.1016/J.JALLCOM.2022.164381.
- [4] P. Geng, M. Morimura, N. Ma, W. Huang, W. Li, K. Narasaki, T. Ogura, Y. Aoki, H. Fujii, Measurement and simulation of thermal-induced residual stresses within friction stir lapped Al/steel plate, J. Mater. Process. Technol. 310 (2022), 117760, https://doi.org/10.1016/J.JMATPROTEC.2022.117760.
- [5] P. Geng, Y. Ma, N. Ma, H. Ma, Y. Aoki, H. Liu, H. Fujii, C. Chen, Effects of rotation tool-induced heat and material flow behaviour on friction stir lapped Al/steel joint formation and resultant microstructure, Int. J. Mach. Tool Manufact. 174 (2022), 103858, https://doi.org/10.1016/J.IJMACHTOOLS.2022.103858.
- [6] L. Zhou, M. Yu, B. Liu, Z. Zhang, S. Liu, X. Song, H. Zhao, Microstructure and mechanical properties of Al/steel dissimilar welds fabricated by friction surfacing assisted friction stir lap welding, J. Mater. Res. Technol. 9 (2020) 212–221, https://doi.org/10.1016/j.jmrt.2019.10.046.
- [7] R. Heuss, N. Müller, W. van Sintern, A. Starke, A. Tschiesner, Advanced Industries: Lightweight, Heavy Impact, McKinsey & Co., 2012, p. 24.
- [8] J. Sun, Q. Yan, W. Gao, J. Huang, Investigation of laser welding on butt joints of Al/steel dissimilar materials, Mater. Des. 83 (2015) 120–128, https://doi.org/ 10.1016/j.matdes.2015.05.069.
- [9] P. Kaushik, D.K. Dwivedi, Effect of tool geometry in dissimilar Al-steel friction stir welding, J. Manuf. Process. (2020), https://doi.org/10.1016/j. imapro.2020.08.007.
- [10] J.M. Piccini, H.G. Svoboda, Tool geometry optimization in friction stir spot welding of Al-steel joints, J. Manuf. Process. (2017), https://doi.org/10.1016/j. jmapro.2017.02.004.
- [11] J.H. Deng, F. Lyu, R.M. Chen, Z.S. Fan, Influence of die geometry on self-piercing riveting of aluminum alloy AA6061-T6 to mild steel SPFC340 sheets, Adv. Manuf. 7 (2019) 209–220, https://doi.org/10.1007/S40436-019-00250-9/FIGURES/22.
- [12] B. Pan, H. Sun, S.-L. Shang, W. Wen, M. Banu, J.C. Simmer, B.E. Carlson, N. Chen, Z.-K. Liu, Z. Zheng, Corrosion behavior in aluminum/galvanized steel resistance spot welds and self-piercing riveting joints in salt spray environment, J. Manuf. Process, 70 (2021) 608–620.
- [13] N. Chen, M. Wang, H.P. Wang, Z. Wan, B.E. Carlson, Microstructural and mechanical evolution of Al/steel interface with Fe2Al5 growth in resistance spot welding of aluminum to steel, J. Manuf. Process. 34 (2018) 424–434, https://doi. org/10.1016/i.jmapro.2018.06.024.
- [14] R. Qiu, H. Shi, K. Zhang, Y. Tu, C. Iwamoto, S. Satonaka, Interfacial characterization of joint between mild steel and aluminum alloy welded by resistance spot welding, Mater. Char. 61 (2010) 684–688, https://doi.org/ 10.1016/j.matchar.2010.03.015.
- [15] Z. Wan, H.P. Wang, N. Chen, M. Wang, B.E. Carlson, Characterization of intermetallic compound at the interfaces of Al-steel resistance spot welds, J. Mater. Process. Technol. 242 (2017) 12–23, https://doi.org/10.1016/j. imatprotec. 2016.11.017
- [16] X. Zhang, X. Zhou, J.O. Nilsson, Corrosion behaviour of AA6082 Al-Mg-Si alloy extrusion: the influence of quench cooling rate, Corrosion Sci. 150 (2019) 100-100, https://doi.org/10.1016/j.corgci.2019.01.030
- 100–109, https://doi.org/10.1016/j.corsci.2019.01.030.
 [17] X. Zhang, Y. Lv, T. Hashimoto, J.O. Nilsson, X. Zhou, Intergranular corrosion of AA6082 Al-Mg-Si alloy extrusion: the influence of trace Cu and grain boundary misorientation, J. Alloys Compd. 853 (2021), 157228, https://doi.org/10.1016/j.jallcom.2020.157228.
- [18] H. Ma, G. Qin, P. Geng, S. Wang, D. Zhang, Microstructural characterisation and corrosion behaviour of aluminium alloy/steel hybrid structure produced by friction welding, J. Manuf. Process. 61 (2021) 349–356, https://doi.org/10.1016/j. imapro.2020.11.014.
- [19] H. Ma, G. Qin, P. Geng, Z. Ao, Y. Chen, Effect of intermetallic compounds on the mechanical property and corrosion behaviour of aluminium alloy/steel hybrid fusion-brazed welded structure, J. Manuf. Process. 75 (2022) 170–180, https://doi. org/10.1016/j.jimapro.2022.01.004.
- [20] Y.C. Lim, L. Squires, T.Y. Pan, M. Miles, J.K. Keum, G.L. Song, Y. Wang, Z. Feng, Corrosion behaviour of friction-bit-joined and weld-bonded AA7075-T6/ galvannealed DP980, Sci. Technol. Weld. Join. 22 (2017) 455–464, https://doi. org/10.1080/13621718.2016.1255404.
- [21] Y. Shi, J. Li, G. Zhang, J. Huang, Y. Gu, Corrosion behavior of aluminum-steel weld-brazing joint, J. Mater. Eng. Perform. 25 (2016) 1916–1923, https://doi.org/ 10.1007/s11665-016-2020-9.
- [22] S.S. Sravanthi, S.G. Acharyya, P. Chapala, Effect of GMAW-brazing and cold metal transfer welding techniques on the corrosion behaviour of aluminium-steel lap joints, Mater. Today Proc. 18 (2019) 2708–2716, https://doi.org/10.1016/J. MATER 2019 07 133
- [23] H. Ma, G. Qin, P. Geng, Z. Ao, Y. Chen, Effect of intermetallic compounds on the mechanical property and corrosion behaviour of aluminium alloy/steel hybrid fusion-brazed welded structure, J. Manuf. Process. 75 (2022) 170–180, https://doi. org/10.1016/j.jmapro.2022.01.004.
- [24] Y. Ma, H. Dong, P. Li, J. Yang, B. Wu, X. Hao, Y. Xia, G. Qi, A novel corrosion transformation process in aluminum alloy/galvanized steel welded joint, Corrosion Sci. 194 (2022), https://doi.org/10.1016/j.corsci.2021.109936.
- [25] P. Geng, H. Ma, M. Wang, G. Qin, J. Zhou, C. Zhang, Y. Ma, N. Ma, H. Fujii, Dissimilar linear friction welding of Ni-based superalloys, Int. J. Mach. Tool

- Manufact. 191 (2023), 104062, https://doi.org/10.1016/J. LJMACHTOOLS.2023.104062.
- [26] S. Xu, D. Xie, G. Liu, K. Ming, J. Wang, Quantifying the resistance to dislocation glide in single phase FeCrAl alloy, Int. J. Plast. 132 (2020), 102770, https://doi. org/10.1016/j.ijplas.2020.102770.
- [27] P. Wang, F. Liu, Y. Cui, Z. Liu, S. Qu, Z. Zhuang, Interpreting strain burst in micropillar compression through instability of loading system, Int. J. Plast. 107 (2018) 150–163, https://doi.org/10.1016/J.IJPLAS.2018.04.002.
- [28] S. Azadehranjbar, B. Wei, D. Xie, K. Ming, J. Wang, J.E. Shield, Strength and plasticity of lamellar vs. fibrous eutectic Mg-Al nanocomposites: an in-situ microcompression study, Acta Mater. 206 (2021), 116624, https://doi.org/ 10.1016/j.actamat.2021.116624.
- [29] Y. Cui, E. Aydogan, J.G. Gigax, Y. Wang, A. Misra, S.A. Maloy, N. Li, In situ micropillar compression to examine radiation-induced hardening mechanisms of FeCrAl alloys, Acta Mater. 202 (2021) 255–265, https://doi.org/10.1016/j. actamat 2020 10 047
- [30] S.J. Wang, D.Y. Xie, J. Wang, A. Misra, Deformation behavior of nanoscale Al-Al2Cu eutectics studied by in situ micropillar compression, Mater. Sci. Eng. (2021) 800, https://doi.org/10.1016/J.MSEA.2020.140311.
- [31] B. Pan, H. Sun, S.L. Shang, M. Banu, P.C. Wang, B.E. Carlson, Z.K. Liu, J. Li, Understanding formation mechanisms of intermetallic compounds in dissimilar Al/ steel joint processed by resistance spot welding, J. Manuf. Process. 83 (2022) 212–222, https://doi.org/10.1016/J.JMAPRO.2022.08.062.
- [32] B. Pan, H. Sun, S.L. Shang, M. Banu, P.C. Wang, B.E. Carlson, Z.K. Liu, J. Li, Understanding formation mechanisms of intermetallic compounds in dissimilar Al/ steel joint processed by resistance spot welding, J. Manuf. Process. 83 (2022) 212–222, https://doi.org/10.1016/J.JMAPRO.2022.08.062.
- [33] B. Pan, H. Sun, S.L. Shang, W. Wen, M. Banu, J.C. Simmer, B.E. Carlson, N. Chen, Z. K. Liu, Z. Zheng, P. Wang, J. Li, Corrosion behavior in aluminum/galvanized steel resistance spot welds and self-piercing riveting joints in salt spray environment, J. Manuf. Process. 70 (2021) 608–620, https://doi.org/10.1016/J. JMAPRO.2021.08.052.
- [34] SORPAS the Welding & Joining Simulation Software, (n.d.)..
- [35] Z. Wan, H.P. Wang, M. Wang, B.E. Carlson, D.R. Sigler, Numerical simulation of resistance spot welding of AI to zinc-coated steel with improved representation of contact interactions, Int. J. Heat Mass Tran. 101 (2016) 749–763, https://doi.org/ 10.1016/j.ijheatmasstransfer.2016.05.023.
- [36] Y. Wang, G. Feng, X. Pu, D. Deng, Influence of welding sequence on residual stress distribution and deformation in Q345 steel H-section butt-welded joint, J. Mater. Res. Technol. 13 (2021) 144–153, https://doi.org/10.1016/j.jmrt.2021.04.059.
- [37] Y. Lu, S. Zhu, Z. Zhao, T. Chen, J. Zeng, Numerical simulation of residual stresses in aluminum alloy welded joints, J. Manuf. Process. 50 (2020) 380–393, https://doi. org/10.1016/J.JMAPRO.2019.12.056.
- [38] K. Zhang, W. Dong, S. Lu, Transformation plasticity of AF1410 steel and its influences on the welding residual stress and distortion: experimental and numerical study, Mater. Sci. Eng., A 821 (2021), 141628, https://doi.org/ 10.1016/j.msea.2021.141628.
- [39] M. Pourbaix, Atlas dEquilibres Electrochimiques, Gauthier-Villars and C, Editeur, Paris, 1963, p. 286.
- [40] H. Niu, S. Niu, A.R. Oganov, Simple and accurate model of fracture toughness of solids, J. Appl. Phys. 125 (2019), https://doi.org/10.1063/1.5066311.
- [41] H. Niu, S. Niu, A.R. Oganov, Simple and accurate model of fracture toughness of solids, J. Appl. Phys. 125 (2019), https://doi.org/10.1063/1.5066311.
- [42] G. Kresse, J. Furthmuller, J. Furthmüller, J. Furthmuller, J. Furthmuller, J. Furthmüller, J. Furthmül
- [43] P.E. Bloechl, P.E. Blöchl, P.E.E. Blochl, P.E. Blöchl, P.E. Bloechl, P.E. Blöchl, P.E. Blochl, P.E. Blöchl, P.E. B
- [44] J.P. Perdew, K. Burke, M. Ernzerhof, Generalized gradient approximation made simple, Phys. Rev. Lett. 77 (1996) 3865.
- [45] A. Jain, S.P. Ong, G. Hautier, W. Chen, W.D. Richards, S. Dacek, S. Cholia, D. Gunter, D. Skinner, G. Ceder, Commentary: the Materials Project: a materials genome approach to accelerating materials innovation, Apl. Mater. 1 (2013), 11002.
- [46] A.O. Lyakhov, A.R. Oganov, H.T. Stokes, Q. Zhu, New developments in evolutionary structure prediction algorithm USPEX, Comput. Phys. Commun. 184 (2013) 1172–1182, https://doi.org/10.1016/j.cpc.2012.12.009.
- [47] N. Chen, H.P. Wang, B.E. Carlson, D.R. Sigler, M. Wang, Fracture mechanisms of Al/steel resistance spot welds in lap shear test, J. Mater. Process. Technol. 243 (2017) 347–354, https://doi.org/10.1016/j.jmatprotec.2016.12.015.
- [48] J. Chen, X. Yuan, Z. Hu, C. Sun, Y. Zhang, Y. Zhang, Microstructure and mechanical properties of resistance-spot-welded joints for A5052 aluminum alloy and DP 600 steel, Mater. Char. 120 (2016) 45–52, https://doi.org/10.1016/j. matchar,2016.08.015.

- [49] J.P. Best, J. Ast, B. Li, M. Stolpe, R. Busch, F. Yang, X. Li, J. Michler, J.J. Kruzic, Relating fracture toughness to micro-pillar compression response for a laser powder bed additive manufactured bulk metallic glass, Mater. Sci. Eng. 770 (2020), 138535, https://doi.org/10.1016/j.msea.2019.138535.
- [50] J.M. Wheeler, ↑ R Raghavan, J. Michler, Temperature invariant flow stress during microcompression of a Zr-based bulk metallic glass, Scripta Mater. 67 (2012) 125–128, https://doi.org/10.1016/j.scriptamat.2012.03.039.
- [51] L. Jiang, N. Chawla, Mechanical properties of Cu6Sn5 intermetallic by micropillar compression testing, Scripta Mater. 63 (2010) 480–483, https://doi.org/10.1016/ i.scriptamat.2010.05.009.
- [52] S. Azadehranjbar, B. Wei, D. Xie, K. Ming, J. Wang, J.E. Shield, Strength and plasticity of lamellar vs. fibrous eutectic Mg-Al nanocomposites: an in-situ microcompression study, Acta Mater. 206 (2021), 116624, https://doi.org/ 10.1016/j.actamat.2021.116624.
- [53] M. Wan, F. Li, K. Yao, G. Song, X. Fan, Theory, method and practice of metal deformation instability: a review, Materials 16 (2023), https://doi.org/10.3390/ Ma16072667
- [54] Y. Ma, H. Dong, P. Li, J. Yang, B. Wu, X. Hao, Y. Xia, G. Qi, A novel corrosion transformation process in aluminum alloy/galvanized steel welded joint, Corrosion Sci. 194 (2022), 109936, https://doi.org/10.1016/J.CORSCI.2021.109936.
- [55] Y. Ma, H. Dong, P. Li, J. Yang, B. Wu, X. Hao, Y. Xia, G. Qi, A novel corrosion transformation process in aluminum alloy/galvanized steel welded joint, Corrosion Sci. 194 (2022), 109936, https://doi.org/10.1016/J.CORSCI.2021.109936.
- [56] F. Mansfeld, Area relationships in galvanic corrosion, Corrosion 27 (1971) 436-442, https://doi.org/10.5006/0010-9312-27.10.436.
- [57] L. Dong, C. Ma, Q. Peng, E.H. Han, W. Ke, Microstructure and stress corrosion cracking of a SA508-309L/308L-316L dissimilar metal weld joint in primary pressurized water reactor environment, J. Mater. Sci. Technol. 40 (2020) 1–14, https://doi.org/10.1016/J.JMST.2019.08.035.
- [58] H. Ming, R. Zhu, Z. Zhang, J. Wang, E.H. Han, W. Ke, M. Su, Microstructure, local mechanical properties and stress corrosion cracking susceptibility of an SA508-52M-316LN safe-end dissimilar metal weld joint by GTAW, Mater. Sci. Eng. 669 (2016) 279–290, https://doi.org/10.1016/j.msea.2016.05.101.
- [59] G. Van Boven, W. Chen, R. Rogge, The role of residual stress in neutral pH stress corrosion cracking of pipeline steels. Part I: pitting and cracking occurrence, Acta Mater. 55 (2007) 29–42. https://doi.org/10.1016/j.actamat.2006.08.037.
- [60] M. Windmann, A. Röttger, I. Hahn, W. Theisen, Mechanical properties of AlXFeY intermetallics in Al-base coatings on steel 22MnB5 and resulting wear mechanisms at press-hardening tool steel surfaces, Surf. Coat. Technol. 321 (2017) 321–327, https://doi.org/10.1016/j.surfcoat.2017.04.075.
- [61] M.T. Laugier, New formula for indentation toughness in ceramics, J. Mater. Sci. Lett. 6 (1987) 355–356.
- [62] R. Lach, L. Antonova Gyurova, W. Grellmann, Application of indentation fracture mechanics approach for determination of fracture toughness of brittle polymer systems, Polym. Test. 26 (2007) 51–59, https://doi.org/10.1016/j. polymertesting.2006.08.006.
- [63] R. Beygi, A.A. Talkhabi, M.Z. Mehrizi, E.A.S. Marques, R.J.C. Carbas, L.F.M. da Silva, A novel lap-butt joint design for FSW of aluminum to steel in teeconfiguration: joining mechanism, intermetallic formation, and fracture behavior, Metals 13 (2023), https://doi.org/10.3390/met13061027.
- [64] W. Wang, T.G. Liu, X.Y. Cao, Y.H. Lu, T. Shoji, In-situ SEM study of crack initiation and propagation behavior in a dissimilar metal welded joint, Mater. Sci. Eng. 729 (2018) 331–339, https://doi.org/10.1016/j.msea.2018.05.077.
- [65] J. Bi, L. Wu, Z. Liu, H. Wang, X. Jia, X. Chen, M.D. Starostenkov, G. Dong, Formability, surface quality and compressive fracture behavior of AlMgScZr alloy lattice structure fabricated by selective laser melting, J. Mater. Res. Technol. 19 (2022) 391–403, https://doi.org/10.1016/J.JMRT.2022.05.051.
- [66] J. Du, Y. Huang, C. Xiao, Y. Liu, Building metallurgical bonding interfaces in an immiscible Mo/Cu system by irradiation damage alloying (IDA), J. Mater. Sci. Technol. 34 (2018) 689–694, https://doi.org/10.1016/j.jmst.2017.10.009.
- [67] H. Xia, L. Li, C. Tan, J. Yang, H. Li, W. Song, K. Zhang, Q. Wang, N. Ma, In situ SEM study on tensile fractured behavior of Al/steel laser welding-brazing interface, Mater. Des. 224 (2022), 111320, https://doi.org/10.1016/j.matdes.2022.111320.
- [68] R. Beygi, R.J.C. Carbas, A.Q. Barbosa, E.A.S. Marques, L.F.M. da Silva, A comprehensive analysis of a pseudo-brittle fracture at the interface of intermetallic of η and steel in aluminum/steel joints made by FSW: microstructure and fracture behavior, Mater. Sci. Eng., A 824 (2021), 141812, https://doi.org/ 10.1016/J.MSEA.2021.141812.
- [69] Q. Chu, T. Xia, P. Zhao, M. Zhang, J. Zheng, F. Yan, P. Cheng, C. Yan, C. Liu, H. Luo, Interfacial investigation of explosion-welded Al/steel plate: the microstructure, mechanical properties and residual stresses, Mater. Sci. Eng., A 833 (2022), 142525, https://doi.org/10.1016/J.MSEA.2021.142525.
- [70] S.L. Shang, H. Sun, B. Pan, Y. Wang, A.M. Krajewski, M. Banu, J. Li, Z.K. Liu, Forming mechanism of equilibrium and non-equilibrium metallurgical phases in dissimilar aluminum/steel (Al–Fe) joints, Sci. Rep. 11 (2021) 1–15, https://doi. org/10.1038/s41598-021-03578-0.